FERMILAB-PUB-16-034-AD
ACCEPTED

Characterisation of the PXIE Allison-type emittance scanner ☆

R. D'Arcy[a,b], M. Alvarez[a], J. Gaynier[a], L. Prost[a], V. Scarpine[a], A. Shemyakin[a]

[a] *Fermi National Accelerator Laboratory, Batavia, USA*
[b] *University College London, WC1E 6BT, UK*

Abstract

An Allison-type emittance scanner has been designed for PXIE at FNAL with the goal of providing fast and accurate phase space reconstruction. The device has been modified from previous LBNL/SNS designs to operate in both pulsed and DC modes with the addition of water-cooled front slits. Extensive calibration techniques and error analysis allowed confinement of uncertainty to the <5% level (with known caveats). With a 16-bit, 1 MHz electronics scheme the device is able to analyse a pulse with a resolution of 1 μs, allowing for analysis of neutralisation effects. This paper describes a detailed breakdown of the R&D, as well as post-run analysis techniques.

Keywords: Particle accelerators, Diagnostics, Beam instrumentation, Allison scanner, Emittance, Phase space, Water-cooled, PXIE

1. Introduction

Various types of emittance scanners have been developed throughout the history of modern beam diagnostics. In this paper we describe the characterisation of an Allison-type emittance scanner [1], developed for use on the PXIE experiment at FNAL [2, 3].

There are several reasons for our choice of device. First, the scan time is shorter than a slit-slit scanner (for example, [4]) thanks to the replacement of the mechanical motion of the second slit by a sweep with an electric field. Then, the rigid emittance scanner box, with fixed relative slit positions, minimises the uncertainty associated with two slits tilting relative to one another.

The electric field between the plates also sweeps low-energy background particles away from the scanner's collector. In addition, the Allison scanner is free from the cross-talk between wires as is often experienced in slit-harp devices [5]. Thus, the increased signal-to-noise ratio of the Allison scanner allows for more effective halo analysis.

Pepper-pot devices (e.g. [6]) provide 4D phase portraits. However, the pre-selected pattern of the holes restricts the range of measured parameters. Also, imaging the beamlets from a low-energy DC beam is difficult.

In the following sections the motivation of the mechanical design choices (including water-cooled housing and stair-cased electric plates), thermal simulations, error analysis, commissioning and functionality, and output are outlined.

2. PXIE

The PXIE accelerator [7] is the front-end test stand of the proposed Proton Improvement Plan II (PIP-II) [8] initiative: a CW-compatible pulsed H^- superconducting linac upgrade to Fermilab's injection complex. The PXIE ion source and Low-Energy Beam Transport (LEBT) section are designed to create and transport a 1–10 mA H^- beam, in either pulsed or DC mode, from the ion source through to the entrance of the RFQ.

Correspondingly, diagnostics are required to provide information about the beam in both DC and pulsed modes of operation. The initial nominal pulse length for PXIE commissioning is 10 μs, chosen as a compromise between the chances of damaging the SRF section and the need for reasonable measurement accuracy of downstream beam instrumentation.

Nominal PXIE LEBT beam parameters are summarised in Tab. 1.

Parameter	Value
Ion energy (H^-), E	30 keV
$\beta(= v/c)$	0.00799
Beam current, I	1–10 mA
Pulse length, t	0.01–16.6 ms
Frequency, f	$\leq$ 60 Hz

Table 1: PXIE LEBT beam parameters.

3. Principles of Operation

The Allison emittance scanner was first proposed in 1983 by Paul. W. Allison *et al.*, developed for use with low-energy H^- ion beams in order to satisfy an angular resolution of less than

☆Operated by Fermi Research Alliance, LLC, under Contract DE-AC02-07CH11359 with the U.S. DOE.

Email address: rtpdarcy@fnal.gov (R. D'Arcy)

Operated by Fermi Research Alliance, LLC under Contract No. De-AC02-07CH11359 with the United States Department of Energy

±0.5 mrad, small errors from space charge, and a compact design [1]. The scanner used at PXIE is a modified version of a SNS model, itself based on an LBNL design [9]. The SNS [10] scanner is designed for a higher beam energy (65 keV) than that of PXIE (30 keV). A pictorial representation of the PXIE emittance scanner can be seen in Fig. 1.

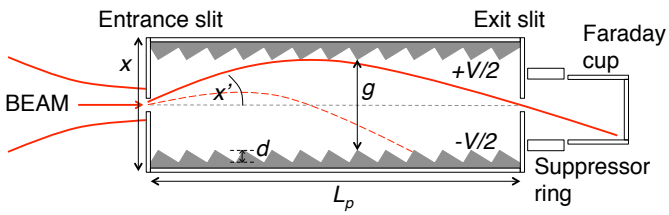

Figure 1: Pictorial representation of the Allison scanner, with an illustration of the bending properties of the electric plates. The deflecting plates are stair-cased with a depth d to prevent impacting particles from being scattered into the back slit.

The beam initially impinges on the front slit of the scanner box with the emerging beamlet passing between a pair of electrically charged deflection plates, driven by two power supplies. The deflector plates are stair-cased in order to prevent impacting particles (and subsequent scattered secondaries) from being passed through the exit slit. At specific plate voltages a portion of the beamlet is deflected such that it is transmitted through the rear slit and onto an emittance scanner (ES) collector. The collector current as a function of the plate voltage is proportional to the beam phase space density as a function of x'. The scanner box is therefore stepped through the beam in order to obtain a full two-dimensional map of the beam in the $x-x'$ phase space.

Assuming that all ions have the same energy while passing between the plates, the slice angle is determined by the voltage V applied across the plates. In approximation of a negligible slit size, particles can pass through both slits only when their initial angle x' with respect to the scanner axis is

$$x' = \frac{V}{U}\frac{L_e}{4g_e} \quad , \qquad (1)$$

where L_e is the effective length of the plates, g_e is the effective gap between the plates, and qU the energy of the ion. The emittance scanner geometric dimensions are summarised in Tab. 2.

In order to determine the angular calibration of the scanner (the effective value of L_e/g_e in Eq. 1, initially provided by SNS and included in their data acquisition package), one can simulate particle tracking through the scanner plates. However, in this instance a method of calibration was used, which employs the dipole correctors installed in each solenoid. This method is described in Sec. 8.

As pointed out in [10], the emittance scanner angular range can be limited by either the available plate voltage or by the geometrical gap. The first limit can be roughly estimated by substituting the effective plate length and gap in Eq. 1 by their geometrical values from Tab. 2, which yields ±0.22 rad. However, the actual limitation for the PXIE scanner comes from the requirement of the ion trajectory to miss the deflection plates.

Parameter	Value
Front slit width, d_1	0.2 mm
Rear slit width, d_2	0.65 mm
Electric plate length, L_p	95.8 mm
Slit-to-slit distance, L_s	118 mm
Geometric plate gap, g	7.4 mm
Sawtooth plate depth, d	1.7 mm
Max. electric plate voltage, $V/2$	1000 V

Table 2: Design parameters of the emittance scanner box.

Taking into account that there is an additional 17 mm longitudinal distance between the entrance slit and the start of the deflecting plates, and an extra 5 mm between the end of the plates and the exit slit, the angular range is in fact approximately ±0.1 rad.

4. Design and Specifications

The SNS Allison-type emittance scanner [10] design was modified to account for the PXIE LEBT beam parameters (see Tab. 1). Different beam energy and current required dimensional alterations to the emittance scanner box. Mechanical additions such as water-cooled front plates were also needed to accommodate DC beam. The following sections outline the choice and reasoning for the design, the validity of simulation in comparison to thermal data, and the safe operational parameters derived from such comparisons.

4.1. Front slit and cooling block

The majority of beam is deposited on the front of the emittance scanner box, with only a small fraction passing through the front slit. The materials selected for this section of the device are chosen to withstand high temperatures and large heating/cooling gradients expected whilst measuring a DC beam. The top and bottom slit plates are made of a molybdenum-based refractory called TZM, composed of 0.5% titanium, 0.08% zirconium, and 99.42% molybdenum. TZM has a relatively low thermal expansion coefficient (5.12×10^{-6} C^{-1} at 126.5 C, approximately three times smaller than stainless steel) and high melting temperature (~2623 C).

The front slits are aligned and bolted to two discrete stainless steel cooling blocks (one for the top slit plate and another for the bottom) with 4.77 mm diameter water cooling channels drilled through. Deionised water flows in series from the supply water line vacuum feedthrough to the top then bottom cooling blocks. The deionised water flows through the channels at roughly 3.0 litres per minute with an average Reynolds number of $\sim 27 \times 10^3$ and a forced convection coefficient of $\sim 21 \times 10^3$ Wm^{-1}K^{-1}.

In order to increase thermal contact a 0.25 mm Sigraflex expanded graphite foil is wedged between the bolted TZM slits and stainless steel cooling blocks.

Four thermocouples are placed near the beam centre to monitor the temperature of both the TZM plate and the cooling block assemblies

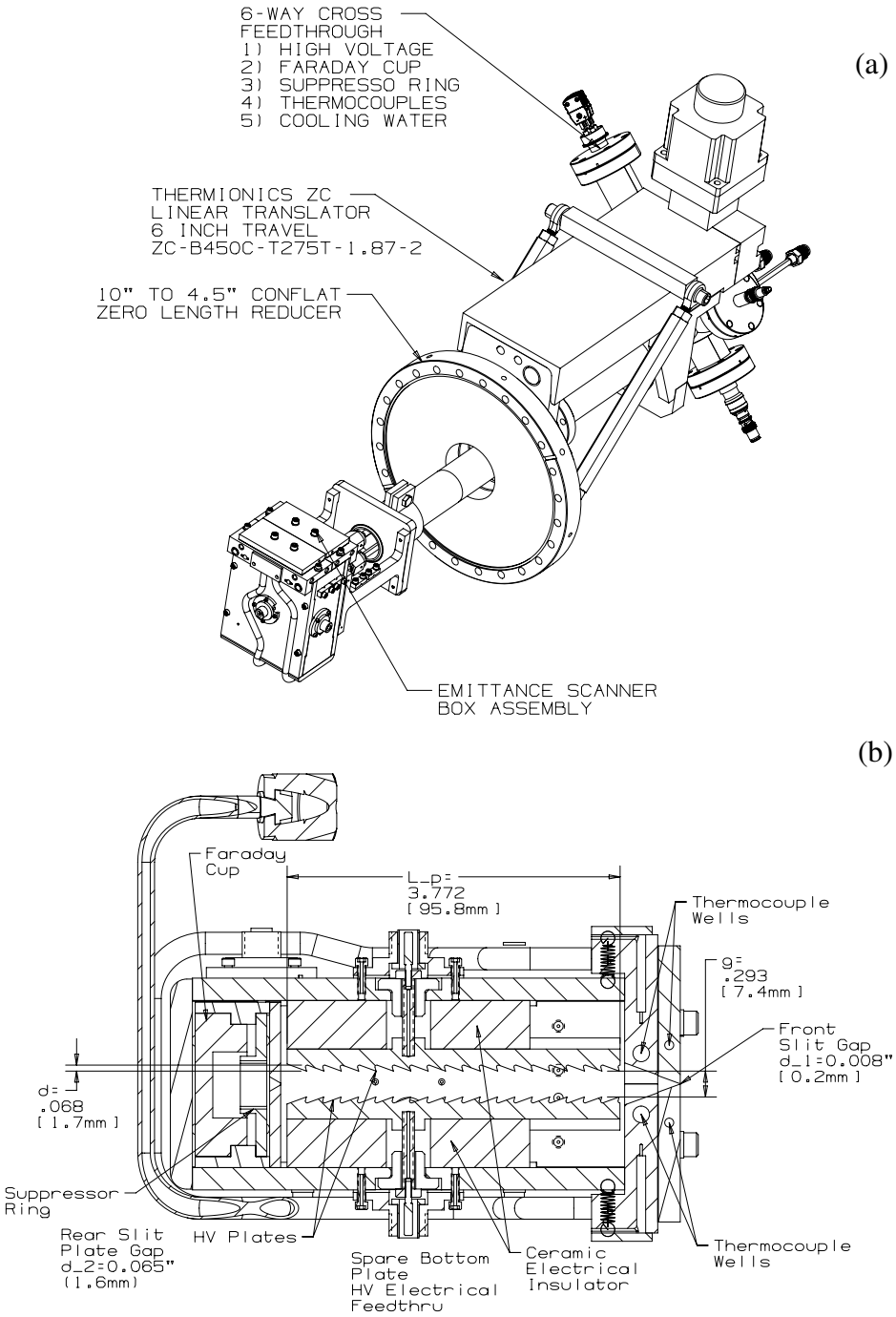

Figure 2: Schematic of the Emittance Scanner a) mechanical assembly, and b) box assembly.

4.2. High voltage elements

To ensure reliable operation up to 1000 V, the high voltage plates are isolated from the body of the emittance scanner with Macor ceramic blocks.

The suppressor ring, biased to −100 V, is used to reduce the flow of secondary electrons escaping the ES collector. Both the suppressor ring and the ES collector are made of OFHC copper and are electrically isolated from ground using Macor ceramic blocks.

4.3. Linear stage

A Thermionics ZC Linear Translator actuates the scanner box assembly with up to 152 mm of travel available. A linear potentiometer is used to measure the exact position of the device as it is inserted into the beam line. A 8718S-01 NEMA 34 Lin Engineering stepper motor drives a 4:1 worm drive gear box with 1.27 mm per turn. An ACME thread drive screw moves the emittance scanner box assembly to its desired location. Limit switches are used to end the specified travel in each direction. In case of a failure of the limit switches a mechanical hard stop is installed on the ACME thread drive shaft preventing the emittance scanner box assembly colliding with the vacuum chamber wall.

4.4. Scanner box

The vacuum compatible materials for the design of the emittance scanner are primarily composed of stainless steel (bellows, flanges, and the six-way cross) and aluminium (the emittance scanner box assembly enclosure). All elements were machined with tight tolerances to ensure the squareness of the box. Furthermore, various tapped holes were made for strain relieving cables as well as to enhance the pumping conductance of the enclosed volume. Vented silver-coated stainless steel fasteners were used throughout the box assembly to reduce trapped pockets of gas.

4.5. Thermal Simulations

A simulation of the thermal stress and expansion of the slits was created in ANSYS to complement, and better understand, measured data. Linear temperature dependent properties were used in the analysis: thermal conductivity, specific heat, thermal expansion, modulus of elasticity, and Poisson ratio.

At the PXIE LEBT beam energy the H^- ions will only penetrate <1 μm. This level of penetration can be considered a surface phenomenon, with the heat flux modelled on the surface of the plates as opposed to volumetrically.

The thermal heat flux was deposited on the slit surface by modelling the beam as a two-dimensional Gaussian distribution, defined by the beam size in each dimension. A Matlab script was used to generate local heat flux points in concentric rings on a surface for a specific beam size and beam current. The data was imported into ANSYS and applied onto the surface of the TZM plates. The mesh was refined in such a way that the heat flux points, when averaged, produced a Gaussian heat flux profile that represents the beam energy deposition. The thermal boundary conditions were defined as convection through the cooling block water channel and thermal contact resistance at the TZM/graphite foil and graphite foil/stainless steel cooling block interfaces. The exposed surfaces of the model were assumed insulated to represent the vacuum space. Radiative heat losses can be ignored because of the low enough temperatures seen on the slit.

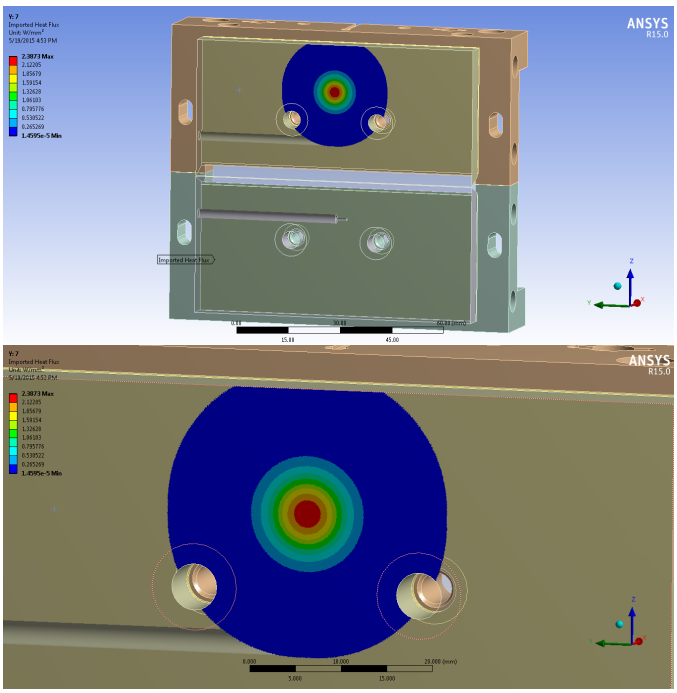

Figure 3: Output from the ANSYS thermal simulation of the slits, demonstrating energy deposition on the top slit and discretised Gaussian heat flux curves.

Structural, as well as thermal, constraints were considered. An adjustable slit gap was a modification made to the FNAL version of the emittance scanner, achieved with a tension spring maintaining positive contact between an adjustment screw and the emittance scanner enclosure. The cooling block was then attached with two screws on each slit, allowing planar freedom orthogonal to the axis of the screws. This structural aspect was included in the code by fixing the adjustment screws in the longitudinal direction; fixing the surface of the cooling block to the enclosure in the transverse plane; applying a 2250 N force to each set of screws clamping the front slit plate to the cooling block; applying a 36 N force to the cooling block at the point of each extension spring.

Once the environment and beam were substantiated the simulation was used to generate data for direct comparison with measurements, testing the validity of each. The simplest method to execute this was to fully deposit a beam, with known size and current, onto either the top or bottom emittance scanner slit. The temperature of the slit was then measured through the output of the thermocouple placed horizontally inside the TZM plate. The temperature readback is compared to that of simulation (with identical beam parameters) as a function of surface heat flux. An example of this data comparison is shown in Fig. 4, with a straight line fitted to both the measured and simulated data. As can be seen the two data sets are in agreement to within

calculated uncertainties.

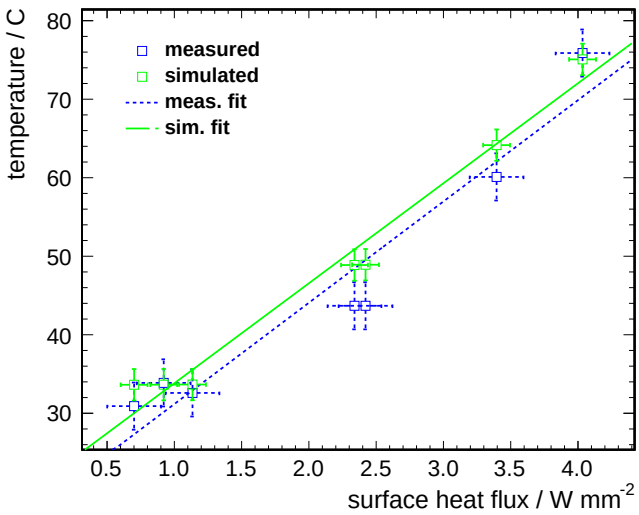

Figure 4: The temperature of the emittance scanner front slit thermocouple wells as a function of the incident power density for both measured and simulated temperatures.

Once the validity of the simulation was demonstrated, the code provided key information about the emittance scanner slits, most pertinently the safe operation limits of the device. Despite the TZM slits having a high melting point and low thermal expansion coefficient, extreme and rapidly changing temperature gradients across any body cause thermal stresses due to differing expansion/contraction forces; as the particle beam is not heating the front slit plates evenly during a scan (due to the stop-start motion of the box) the temperature gradients through the front slit, and subsequently the cooling block, cause thermal stresses which can lead to fission if significantly high.

The plot in Fig. 5 shows the simulated maximum stress induced in the cooling block as a function of its surface heat flux for a range of beam spot sizes. In this case the cooling block temperature, T_{cb}, was monitored rather than that of the TZM plates as the cooling block has a lower strength and is therefore more liable to break under beam stresses. In each simulation, like those in Fig. 4, a double-Gaussian distribution beam – with preset size, current, and energy – was fully deposited on the top/bottom slit of the emittance scanner. The resulting stress on the cooling block is plotted against the surface heat flux from such a beam, indicating whether this regime falls short, meets, or exceeds known mechanical limits of the cooling block. This plot may be used as a vital runtime document providing instant visualisation as to whether the operating parameters will result in safe operation (green), possible deformation (yellow), or probable fissure (red) of the cooling block.

5. Electronics and Motion Control

A block-diagram layout of the emittance scanner data acquisition (DAQ) and controls system is shown in Fig. 6. This system consists of deflector plates and suppressor high-voltage, motion control, and ES collector signal acquisition. The entire

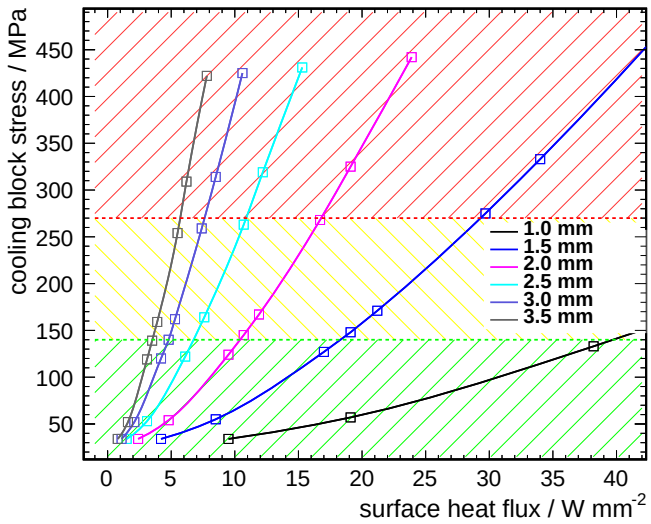

Figure 5: Thermal stress curves as a function of surface heat flux for a series of RMS beam sizes. The shaded regions represent the safe operation (green, T_{cb}<39 C), possible deformation (yellow, T_{cb}<49 C), and probable fissure (red, T_{cb}>49 C) regimes for the copper cooling block.

system is operated by a LabVIEW-based software package in a rack-mount Windows PC.

5.1. High Voltage Systems

The emittance scanner deflector plate high-voltage is supplied by two independent Kepco BOP 1000M bipolar four-quadrant power supplies. These units are fast, low-noise, and low-ripple supplies that can operate bidirectionally from zero to a maximum output voltage of ±1000 V. They have a closed loop gain of 100 V per volt, a slew rate of 12 V per microsecond, and a large signal frequency response of up to 1.9 kHz. Under nominal beam operations, we step the voltage on these units at up to 60 Hz, well below their bandwidth limit.

The secondary electrons from the ES collector are inhibited by the field of the suppressor electrode. Beam studies show that the ES collector signal plateaus at a voltage greater than −50 V. In turn, we operate this suppressor voltage at −100 V, which is generated by a TDK-Lambda GEN750W 150 V power supply.

5.2. Motion Control

The motion of the emittance scanner box is operated via a LabVIEW controls interface installed on a Windows PC. The PC utilises a four-axis stepper motor control board (National Instruments PCI-7334) to generate all of the motor signals. The emittance scanner motion utilises a stepper motor to drive a linear stage (Thermionics ZC-B450C-T275T-1.87-2) with a maximum travel distance of 152 mm and an overall single step resolution of 3.2 μm. A rotary encoder attached to the stepper motor allows us to operate the motion control system in closed-loop mode to ensure accurate relative motion. Motion was tested using a rotary spring gauge which shows a position resolution of <12 μm. To help eliminate the effects of mechanical backlash, all emittance measurements are made with motion restricted to only a single direction.

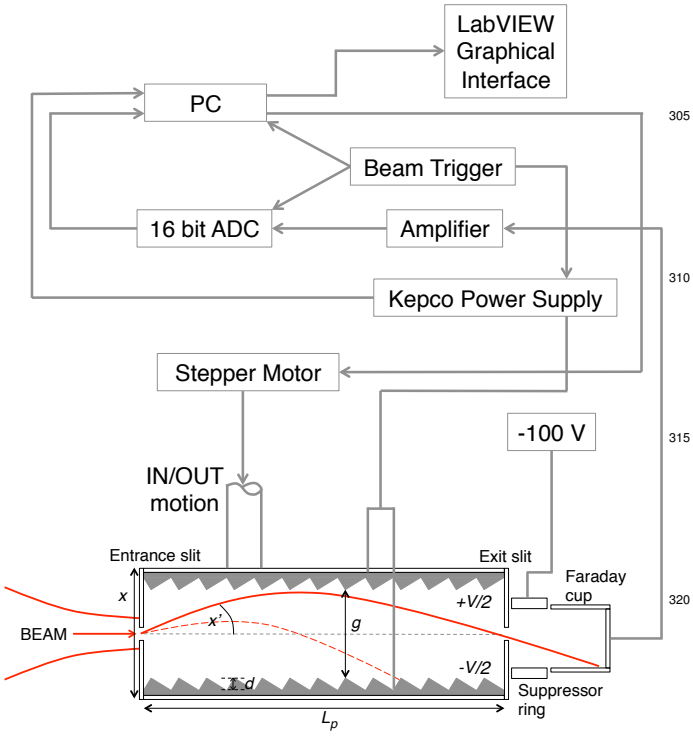

Figure 6: Schematic of the emittance scanner hardware as related to the running of a scan.

5.3. *Data Acquisition and Operation*

The beam current measured by the ES collector is converted using a low-noise current-to-voltage preamplifier. This preamplifier has a gain of 10^5 volts per amp and a bandwidth of 350 kHz. This signal is then sampled using a 1 MHz, 16-bit ADC (National Instruments, PCIe-6351) with an input range of −10 to +10 V. An on-board FIFO memory allows for data buffering and continuous streaming of measurements to the LabVIEW acquisition software. This allows for time-sliced emittance measurements over a single measurement scan.

6. Scanner in Operation

The front panel of the LabVIEW runtime package (written by colleagues at SNS to control the HV supplies and stepper driver, and read the thermocouples and ES collector signals [11]) allows for the choice of scan parameters e.g. the transverse positional and angular range, the number of steps taken within that range, and the width of each step. The machine is re-homed after each scan in order to reset the step count to zero. Assuming instantaneous velocities, the time taken for a scan may then be defined as

$$t \approx \frac{2}{v}\left(x_1 + n_x w_x\right) + \frac{n_x n_{x'}}{f} \quad , \qquad (2)$$

where v is the velocity of the motor and f is the sweeping frequency of the electric plates (typically set at 1.5 mm s^{-1} and 60 Hz), x_1 is the scan start position relative to home, n_x and $n_{x'}$ are the number of steps in position and angle, and w_x and $w_{x'}$ are the width of said steps. A customary pixel size is 1 mm × 1 mrad. With these widths, and a scan range of ±30 mrad and ±25 mm, the time taken to complete a scan (including insertion and re-homing) is 2.5 mins.

Due to the dual-functionality of the PXIE ion source the emittance scanner is also required to operate in both pulsed and DC modes. Operation in pulsed mode is preferable at the commissioning stage to decrease the chances of damage to the emittance scanner from high duty factors. The LabVIEW runtime package was expanded to operate in both DC and pulsed modes, separating the structure of each timing window into individual time slices for both modes (the slices being identical in DC to within known statistical fluctuations). Each timing window is sampled at a rate of 1 MHz so, for example, a slice size of 10 μs would produce an array of data averaged across 10 measurements.

This functionality may be used to assess the evolution of the phase portrait through the pulse. The plot in Fig. 7 contains one such example, demonstrating how the phase space rotates due to neutralisation of the beam, reaching a steady-state seemingly by the 12th time slice, i.e. 1.5 ms.

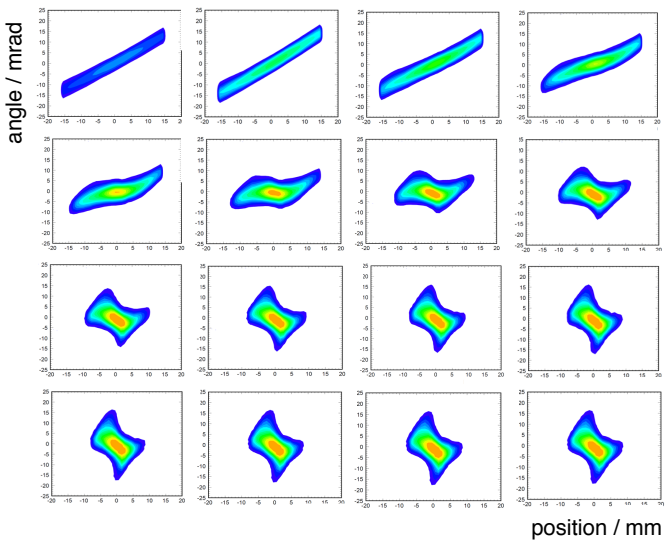

Figure 7: Evolution of the the phase space portrait as stepping through a 2 ms, 5 mA H$^-$ beam. The magnitude of the z-axis is kept constant across all plots, ranging from low ES collector signal (blue: 0–10 μA) to high signal (orange: 100–110 μA) regions. Similarly, the axis limits for each plot are identical, ranging from −20 to +20 mm horizontally and −25 to +25 mrad vertically. The order of time (between 0.125 ms slices) begins at the top left, processes left to right, ending in the bottom right portrait.

This aspect of the code may also be used to monitor the evolution of a pulse's intrinsic properties. An example of this is shown in Fig. 8a, comparing the evolution of the normalised emittance of a 2 ms pulse (sampled with 50 μs slices) with a DC beam. The emittance falls as the pulse extends due to neutralisation of the beam. The plateau value at the end of the pulsed beam is the same as that of the fully neutralised DC beam (to within expected ion source fluctuations or emittance scanner errors).

The same effect can be seen for the Twiss parameters in

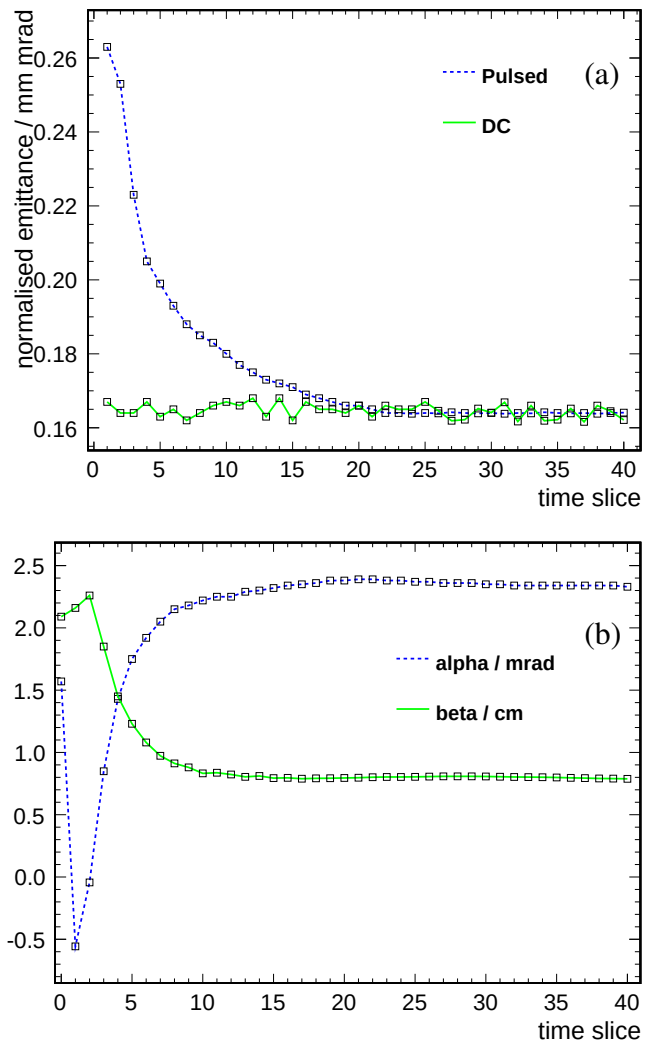

Figure 8: The evolution of a) normalised emittance for a pulsed and DC beam, and b) Twiss alpha and beta, as stepping through a 2 ms 5 mA pulse.

Fig. 8b, where large variations are seen in the first 600 μs of the pulse (the Twiss alpha flips polarity) before the parameters plateau, again due to neutralisation.

In pulsed mode the instrumental background is subtracted using the data recorded before or after the beam pulse – the default time window is typically 100-200 μs. In DC mode an average value is taken of the floor of each time slice (where no beam is present) then subtracted from each data point, equivalent to a pedestal subtraction.

7. Output Example

Once the scanning process is complete the data is saved to a file (in spreadsheet format) on a Windows PC. This data (after bias subtraction and centring) may then be put through any one of a number of algorithms in order to determine the beam emittance and other important parameters (e.g. Twiss functions).

Figure 9 gives an example of a 5 mA beam phase space portrait taken towards the end of a 2 ms pulse after applying such a procedure. The normalised RMS emittance value (with a 1% threshold cut) for this distribution is calculated to be $\varepsilon_N = 0.135$ mm mrad.

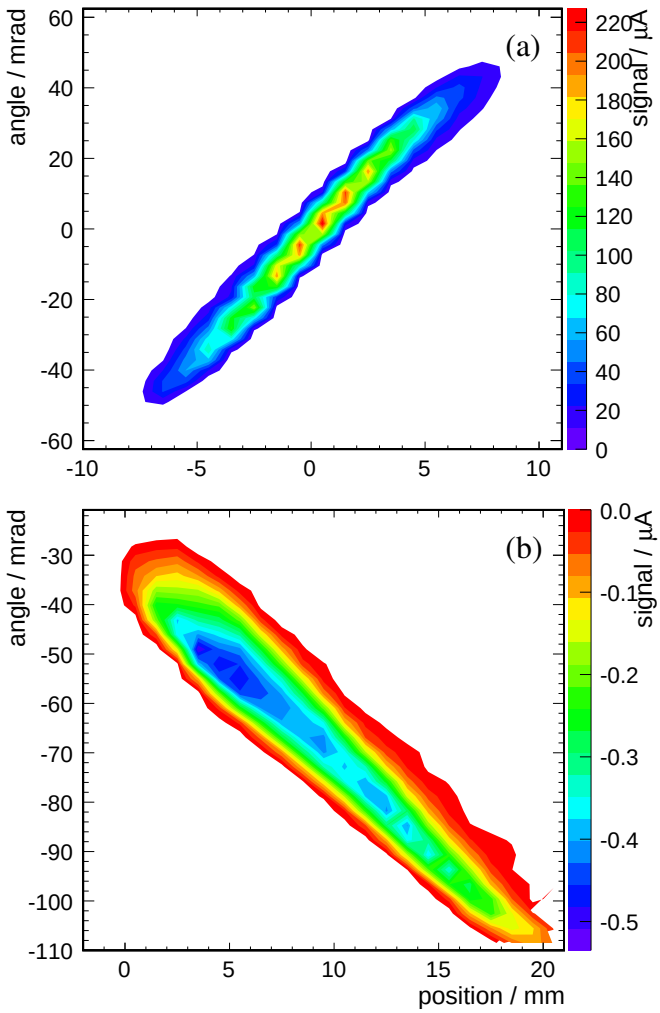

Figure 9: The phase space as recorded by the Allison scanner at the end of the beamline, for a) a 5 mA H^- beam, and b) the associated positive signal. Note the change in signal scale and axis range for each plot. This data set was recorded using a 1 mm × 1 mrad matrix. In each case a threshold cut of 1% of the maximum signal was taken. However, for the proton plot – as the signal has the opposite polarity to that of the H^- – this is effectively a cut of −1%. It is important to note that this data set was selected as the beam steering effects of the beam line result in a clear separation in phase space between the positive H^- signal and negative p^+ signal.

All emittance values quoted in this paper are calculated with a 1% cut. Obviously, the cut takes out not only electronic noise etc. but part of the beam as well, decreasing the reported RMS emittance from its true value. To estimate an order of magnitude of the effect, one can calculate this decrease for a Gaussian beam. The ratio η of the RMS emittance reported after a cut of μ to the RMS value of the entire Gaussian beam is

$$\eta(\mu) = 1 - \mu\,(1 - \ln\mu) \quad , \tag{3}$$

In Fig. 10, the red curve shows Eq. 3 tied to the measured 1% cut point. For the cut chosen in this paper ($\mu = 1\%$) Eq. 3 gives

$\eta = 0.945$, i.e. underestimating (in this model) the emittance by 5.5%.

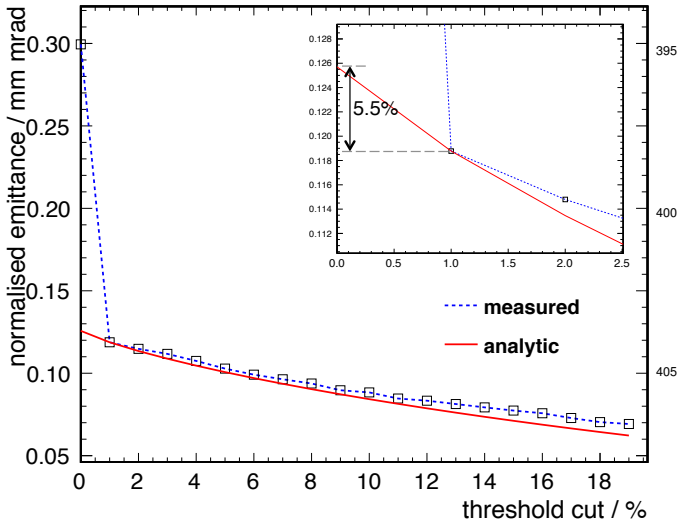

Figure 10: The normalised RMS emittance as a function of threshold cut (as a percentage of the maximum signal). There is an obvious inflection point at 1%, thus chosen for normalisation with the analytic form. The inset is a magnification of this inflection point, demonstrating the percentage difference between the measured 1%-cut emittance and the analytic 0%-cut emittance for a double-Gaussian beam.

The emittance scanner electronics use a ±10 V, 16-bit ADC. As an illustration of the dynamic range of the device, Fig. 9b shows a phase space distribution that corresponds to the ES signals with polarity opposite to those that lead to Fig. 9a. These signals, ~400 times smaller than in Fig. 9a, are interpreted as protons, created immediately downstream of the ion source extraction region through charge-exchange of the primary H^- ions with residual gas. Note that the sign of the voltage-to-angle conversion in Fig. 9 was not changed for the plot representing the protons. The typical RMS value of the noise (fluctuation of the values recorded far from the beam) is 17 nA for 5 μsec bins. If one considers 3 RMS values as the signal cut limit, the dynamic range is ~2000.

8. Calibration and Errors

8.1. Equipment Uncertainties

As previously mentioned the position of the emittance scanner box is known to within ±0.012 mm (±4 motor steps), equivalent to the resolution of a rotary spring gauge. Mechanical slippage was demonstrated to be negligible to within this error.

The rotary encoder, attached to the back of the motor, accounts for any missed steps from the driver to the motor, nullifying this systematic error.

The emittance scanner electric plates are controlled by a Kepco power supply. They each have a resolution of ±0.5 V.

8.2. Angular Calibration

The Allison scanner angular position of a phase space pixel is derived from the voltage on the deflecting plates according to Eq. 1. Thus, the coefficient of proportionality between the angle and the voltage is determined by the particle's energy and the ratio between the effective electric plate length and gap, which may differ from their mechanical values. A method of direct measurement of this coefficient, using the dipole correctors built into each solenoid, was employed.

First, the correctors were independently calibrated to several percent accuracy, and combinations of their currents that move the beam in vertical or horizontal directions at the location of the scanner were determined. Then, with the scanner mounted vertically, the phase portraits were recorded at various vertical beam positions, and the position and angular centroids of the distributions ($\langle x \rangle$ and $\langle x' \rangle$, respectively) were calculated [12]. The corrector kick results in shifts of both centroids that are geometrically related as

$$\Delta\langle x' \rangle = \frac{\Delta\langle x \rangle}{L_d} \quad , \tag{4}$$

where L_d is the drift length between the magnetic centre of the solenoid correctors and the entrance slit, and $\Delta\langle x \rangle$, $\Delta\langle x' \rangle$ are shifts of the position and angular centroids respectively.

Initially, the coefficient of proportionality between the angle and the plate voltage is calculated from the mechanical dimensions of L_p and g. Then the fitted slope of the measured centroids, $\langle x' \rangle = f(\langle x \rangle)$ (see Fig. 11), is compared with the measured value of the drift length between the solenoid correctors and the entrance slit, $L_m = 1.08 \pm 0.01$ m. For this procedure the distance derived from the linear fit is $L_d = 1.18 \pm 0.02$ m. The coefficient of proportionality between the angle and plate voltage is therefore scaled by an additional factor $\alpha = L_d/L_m = 1.09 \pm 0.02$.

The calibration error is the primary known systematic contribution to the emittance. This ±2% uncertainty is therefore introduced to all calculated emittance values via $\sigma_\varepsilon/\varepsilon = \sigma_\alpha/\alpha$

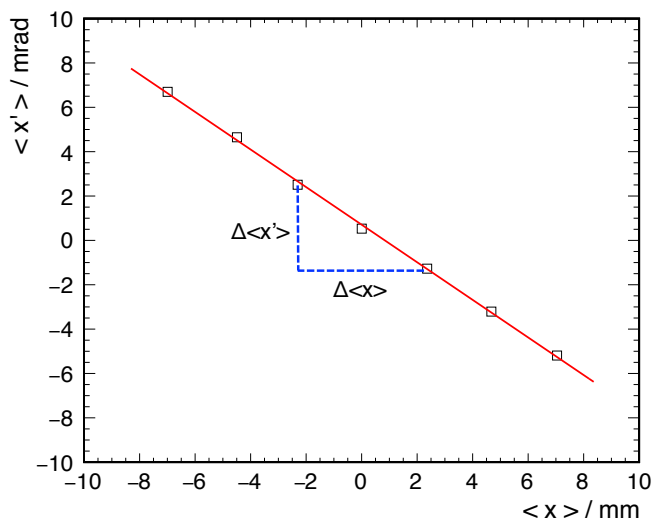

Figure 11: Phase space shifts of the centroids ($\langle x \rangle, \langle x' \rangle$) caused by the vertical kicks of the solenoid dipole correctors. The red line denotes the linear fit of $\langle x' \rangle = f(\langle x \rangle)$ used for calibration of the angular component of the Allison scanner.

Note that the described method relies only on accurate calibration of the scanner motion and on the measured distance between the centres of the correctors and the front slit of the Allison scanner. The corrector calibration is used only to provide the beam position at the centre of the Allison scanner.

8.3. Thermal effects

The simulations outlined in Sec. 4.5 suggest a thermal expansion of the front plates of the emittance scanner due to beam energy deposition. This expansion would decrease the front slit gap width, reducing the signal reaching the ES collector.

This hypothesis was tested by placing the emittance scanner in the centre of the beam line, centring and collimating the beam, then switching on the beam to analyse the signal reaching the ES collector as a function of time. In these studies a 5 mA, 3 mm RMS beam was pulsed at 60 Hz with the average power density varied by altering the pulse length i.e. duty factor.

Figure 12 shows the signal decay at a duty factor of 95%. An exponential of the form $V = A + Be^{-t/\tau}$ is fitted to the data, where $(1-A)$ defines the percentage drop associated with slit expansion. In this example, with the maximum signal normalised to 1.0 for ease of interpretation, the associated signal drop is 4.7%.

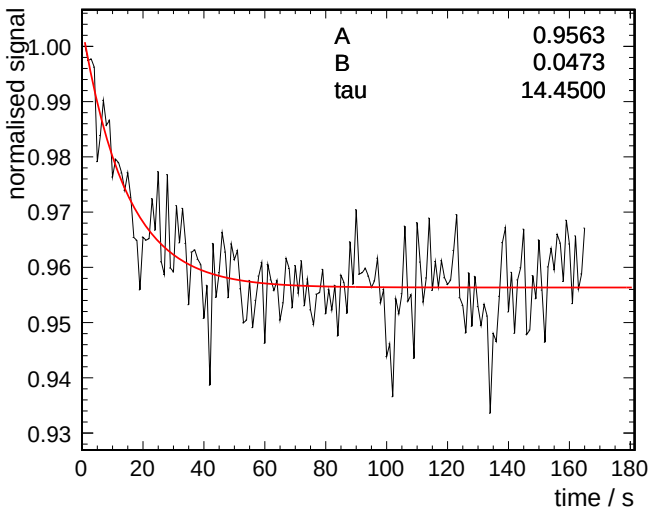

Figure 12: The signal drop at the ES collector due to thermal expansion of the front slits from the energy deposition of a 5 mA H^- beam. The signal is normalised to 1.0 to easily identify the percentage drop.

The beam is switched off and, once the slit temperature equilibrates to room temperature, the process is repeated for different duty factors. Table 3 shows this drop for a range of duty factors. The overall percentage drop as a function of duty factor follows an approximately linear relation, as expected from simulation, with the largest drop at the highest duty factor. Also, the intrinsic thermal timing constant of the slits is held approximately constant for each case, irrespective of duty factor – again as expected. Results of Tab. 3 show that depositing the beam at maximum power doesn't dramatically affect the entrance gap size.

Duty Factor	Signal Drop	Timing Constant
5%	0.0%	14.4 s
25%	1.3%	14.7 s
50%	2.1%	14.5 s
75%	3.5%	14.4 s
95%	4.7%	14.3 s

Table 3: Percentage drop in signal reaching the ES collector for a range of duty factors (with a 5 mA H^- beam). The time constant of the TZM front plate and cooling block remains approximately constant at 14.5 s as expected from simulations.

In order to asses the effect of slit expansion as a function of rate of energy deposition, an emittance measurement was repeated with identical scan parameters (acquisition window, timing, etc.) for a range of duty factors. The emittance was then calculated in each case, with the results shown in Fig. 13. As can be seen the emittance remains constant across the full range to within known sources of error.

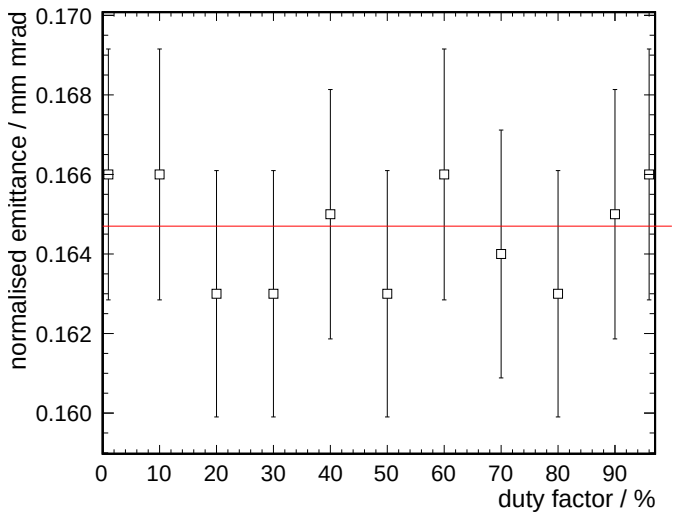

Figure 13: RMS emittance as a function of duty factors for a 5 mA H^- beam. The errors represent the systematic uncertainty from calibration. It should be noted that, despite similar beam parameters, the emittance values in this plot differ to those in Fig. 9 due to different ion source and solenoid tune.

8.4. Space charge effects

Once the beamlet has passed through the front slit space charge may increase its size at the back slit, increasing, as a result, the measured angular width. It is possible to calculate the maximum relative increase of the beamlet height in the model of a flat, constant-density beam, neglecting its expansion due to thermal velocities. For a beam that has a Gaussian spacial distribution, with RMS radius σ_x, the maximum electric field at the surface of the sheet formed by the front slit is

$$E_s = \frac{I_{bl}}{2\pi\,\sigma_x^2\,\beta c\,2\varepsilon_0}\,d_1 \quad , \tag{5}$$

where d_1 is the width of the front slit and I_{bl} is the current of the beamlet penetrating the front slit.

After passing a distance L_s between the two slits, the boundary ions are shifted by

$$\Delta y = \frac{eE_s}{m_i}\frac{1}{2}\left(\frac{L_s}{\beta c}\right)^2 \quad , \tag{6}$$

where m_i is the mass of the ion. Therefore, the increase of the beamlet height normalised by the initial height value, d_1, is

$$\begin{aligned}\frac{2\Delta y}{d_1} &= \frac{eI_{bl}}{(\beta c)^3\, m_i}\frac{1}{4\pi\varepsilon_0}\left(\frac{L_s}{\sigma_x}\right)^2 \\ &= \frac{P_b}{2P_o}\left(\frac{L_s}{\sigma_x}\right)^2 \quad ,\end{aligned} \tag{7}$$

where P_b is the beam perveance and $P_o \equiv 4\pi\varepsilon_0\sqrt{\frac{2e}{m_i}} = 1.54\frac{\mu A}{V^{3/2}}$. For typical PXIE parameters ($P_b = 0.001\frac{\mu A}{V^{3/2}}$, $L_s = 118$ mm, $\sigma_x = 3$ mm) the relative increase is 0.5. As is shown in Sec. 8.5, the beamlet height at the rear slit is $\gg d_2 > d_1$ and, therefore, the contribution from space charge is negligible.

8.5. Error related to the finite slit size

The slit width affects the measurement accuracy of the scanner due to the angular cut introduced. Increasing the slit width decreases the resolution of the emittance measurement, therefore increasing the measured emittance by a factor dependent on the Twiss values of the beam [14, 15]. Assuming a Gaussian beam, the additional beam incident on the ES collector resulting from this can be quantified as a function of slit size. This percentage emittance growth is defined as

$$\begin{aligned}\frac{\varepsilon_m - \varepsilon_t}{\varepsilon_t} = \Bigg(1 - \frac{1}{\varepsilon_m}\Bigg(\beta_m\frac{d_1^2 + d_2^2}{12L_s^2} + \frac{1+\alpha_m^2}{\beta_m}\frac{d_1^2}{12} \\ -\alpha_m\frac{d_1^2}{6L_s}\Bigg) + \frac{1}{\varepsilon_m^2}\frac{d_1^2 d_2^2}{144L_s^2}\Bigg)^{-\frac{1}{2}} - 1 \quad ,\end{aligned} \tag{8}$$

where subscripts 't' and 'm' represent true and measured parameters, respectively (see [14] for a comprehensive derivation, in which case Eq. 8 takes on a slightly different form due to the paper's definition of d_1 and d_2 as half slit widths).

As a numerical example of the effect, the error in measured emittance using dimensions of the PXIE Allison scanner box ($d_1 = 0.2$ mm, $d_2 = 0.65$ mm, and $L_s = 118$ mm), with typical beam parameters at the end of the PXIE LEBT ($\alpha_m = -0.56$ rad, $\beta_m = 0.33$ m, and $\varepsilon_m = 14.4$ mm mrad), is 3.5%.

8.6. Discussion of errors

The choice of the acquisition grid size (x mm $\times$ y mrad) is dependent on the size of the beam and the speed of acquisition (particularly the latter if the beam properties have the tendency to drift). For these reasons the vast majority of data was acquired with a grid resolution of 1 mm $\times$ 1 mrad. In order to check that this choice does not lead to a systematic increase/decrease of the reported emittance, several phase space distributions were acquired with twice the step resolution in position and/or angle (e.g. 0.5 mm $\times$ 1 mrad). For all data the reported emittance was within 1% of that obtained with the default grid.

Similarly, it was verified that the position of the beam impinging upon the front slit was not introducing systematic errors in the determination of the beam emittance. Again, to within 1%, the reported emittance did not depend on steering, as long as the entire beam is intercepted by the front slit in the direction perpendicular to the plane of measurement, which is easily verified by comparing the sum of the signals over the entire phase space.

Finally, the statistical uncertainty was estimated by repeated measurements under the same conditions over many hours. In this case, we found that the standard deviation of the reported emittance was < 1%.

Thus, altogether, random measurement errors (also including voltage non-linearities and electronics noise) account for approximately ±1% (RMS). Table 4 displays a numerical example of the total effect of the uncertainties outlined in this section for a beam with parameters defined at the end of Sec. 8.5. Note that, as discussed in Sec. 7, the uncertainty resulting from the choice of cut may be at the 5% level.

Source	Contribution
Calibration error	±2%
Statistical fluctuations	< 1%
Slit size effects	−3.5%
Total error	+2.1% −4.1%

Table 4: A numerical example of the sources and contributions of error for the normalised emittance for the case described in Sec. 8.5.

9. Unresolved Matters

While several sources of error have been identified and estimated in the previous section, some measurements remain difficult to interpret from a beam dynamics point of view alone, thus prompting questions about the validity of the reported emittance under certain conditions. In particular, at the end of the LEBT, the emittance measured with the Allison scanner (plotted as a function of the third solenoid current) has a characteristic 'V-shape' (see Fig. 14), most notably when the minimum measured emittance is lowest. Part of this correlation can be attributed to the finite size of the scanner slits as described in Eq. 8. In order to make this relation more apparent, Eq. 8 can be re-written such that the measured emittance is a function of the RMS beam sizes σ_1 and σ_2 that the beam would have at the front and rear slits. Correspondingly (ignoring space charge):

$$\varepsilon_m^2 = \varepsilon_t^2 + \sigma_1^2\frac{d_2^2}{12L_2^2} + \sigma_2^2\frac{d_1^2}{12L_2^2} + \left(\frac{d_1 d_2}{12L_s}\right)^2 \quad . \tag{9}$$

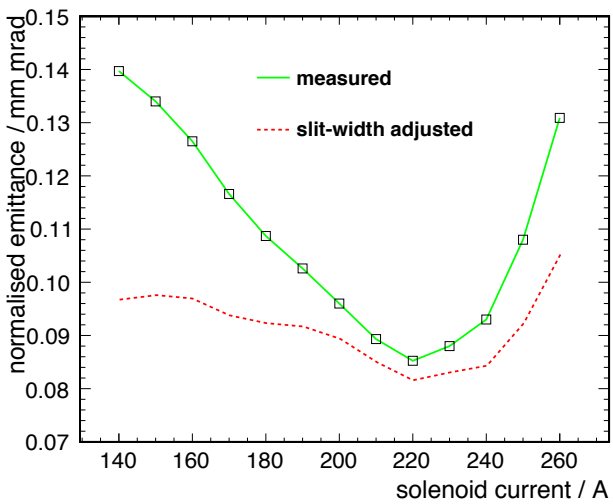

Figure 14: The measured normalised emittance as seen at the Allison scanner as a function of solenoid three current. The emittance is then manipulated using the relation in Eq. 8 to demonstrate the artificial emittance growth from finite slit-size effects.

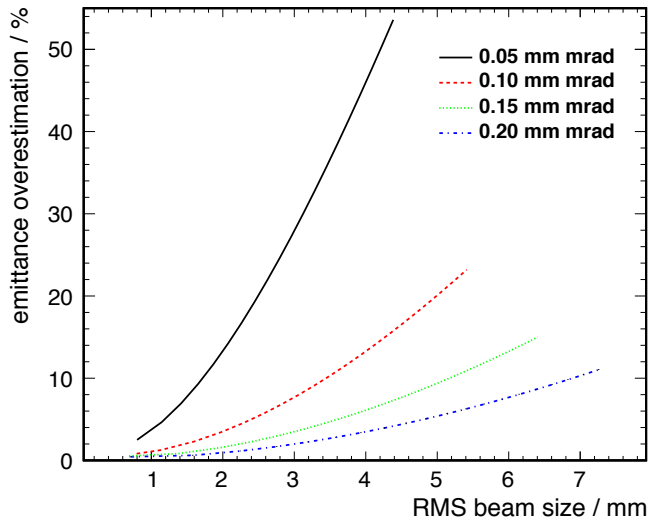

Figure 15: Overestimation of the measured emittance with respect to the true emittance as a function of the measured beam size. The overestimation is calculated using the relation in Eq. 9, with $\alpha = 0$ in all cases.

In this form, the correction terms have clear physical meanings. The first term is a product of the beam size at the first slit and the RMS angular scatter measured for a zero-emittance beam due to the finite size of the second slit; the second term is the same but with the beam size now taken at the second slit and the RMS angular scatter a result of the finite size of the first slit; the third term (usually negligible) is a correction that corresponds to the measurement of a pencil-like beam.

Thus, Eq. 9 shows that the correction terms are sensitive to the beam size at the location of the emittance scanner, while in the form in Eq. 8 better reveals that the smaller the true emittance, the larger the effect of the finite slit size on the measured emittance. Both points are illustrated in Fig. , where for four distinct values of the true emittance, the overestimation from the measured emittance due to the finite size of the slits is plotted against the beam size.

Once corrected for the finite slit size, one would expect the emittance to be constant for low solenoid current values, and to increase for cases where the beam experiences a small waist. This in turn results in some emittance growth at the location of the measurement due to space charge. While this is somewhat true when applied to the data from Fig. 14 (red dashed curve), for other data sets the correction from the finite slit size is too small to eliminate the 'V-shape'.

So far, attempts to attribute the remaining discrepancy between measurements and expectations to other possible sources (e.g.: changes of the emittance scanner head pitch angle during its travel through the beam) have been unsuccessful. Meanwhile, PIC simulations show that it is possible to observe a minimum on an emittance versus 3rd-solenoid current plot, although the magnitude of the emittance variations is smaller than what we obtain for the measured data after correction.

Therefore, presently, we do not exclude that the behaviour of the corrected measured emittance in Fig. 14 is the result of some beam transport dynamics inadequately understood at this time.

10. Conclusions

A water-cooled Allison-type phase space and emittance scanner able to run in DC and pulsed mode has been designed and commissioned for PXIE at FNAL. Effective implementation and running of such a device has been demonstrated, with thermal anlyses providing a blueprint for safe operation of this and similar future devices. Data acquisition is quick (<3 min for a scan of size 60 mrad × 50 mm), and the scanner produces high-resolution phase space reconstruction from both high- and low-magnitude signals. An emittance value is delivered to a narrow level of precision (typically <5% for nominal PXIE beam parameters, as outlined in Sec. 8 and discussed in Sec. 9) for this type of device thanks to a rigorous error analysis and novel calibration techniques. With these factors, and the time slice functionality, the scanner has played a crucial role in the optimisation of the PXIE LEBT beam line and will continue to provide essential data in the future stages of the experiment.

11. Acknowledgements

Thanks go to Martin Stockli, Willem Blokland, *et al.* at SNS for their collaboration in modifying the Allison scanner design, providing their version of the LabVIEW operation code and also in their assistance in the assembly and commissioning. The scanner software was updated by D. Slimmer. Authors acknowledge contributions of B. Hanna (measurements and maintenance), J.-P. Carneiro (simulation and measurements), W. Marsh (scanning programs), as well as A. Saewert, A. Ibrahim, B. Fellenz (electrical engineering support), and S. Sylejmani (mechanical support).

The work outlined in this paper was operated by Fermi Research Alliance, LLC, under Contract DE-AC02-07CH11359 with the U.S. DOE.

References

[1] P. Allison, J. Sherman, D. Holtkamp, *An emittance scanner for intense low-energy ion beams*, Trans. Nucl. Sci. **NS-30** 4 (1983).

[2] A. Shemyakin *et al.*, *Status of the Warm Front End of PXIE*, Proc. of LINAC14, Geneva, Switzerland (2014), THPP056.

[3] V. Lebedev *et al.*, *An 800 MeV Superconducting Linac to Support Megawatt Proton Operations at Fermilab*, Proc. of LINAC14, Geneva, Switzerland (2014), THIOA05.

[4] A. Anders, E. Chacon-Golcher, *Time resolved emittance of a bismuth ion beam from a pulsed vacuum arc ion source*, J. Appl. Phys. **93** 2298-2300 (2003).

[5] A. Zhukov *et al.*, *Transverse Emittance Measurements in MEBT at SNS*, Proc. of LINAC2010, Tsukuba, Japan (2014), TUP089.

[6] Y. Yamazaki *et al.*, *High-precision pepper-pot technique for a low emittance electron beam*, Nucl. Instrum. Meth. A **322** 139-145 (1992).

[7] *PXIE Design Handbook*, Project X Doc. 1148-v5, `http://projectx-docdb.fnal.gov/cgi-bin/ShowDocument?docid=1148`

[8] *The PIP-II Reference Design Report*, `http://pip2-docdb.fnal.gov/cgi-bin/ShowDocument?docid=1`

[9] M. Stockli, R. F. Welton, R. Keller, and M. Leitner, *Emittance studies with an Allison scanner*, Review of Scientific Instruments, Volume 77, Issue 3, (2006)

[10] M. Stockli *et al.*, *Low-energy Emittance Studies with the new SNS Allison emittance scanner*, Proc. of PAC09, Vancouver, Canada (2009), TH6REP012.

[11] C. D. Long *et al.*, *Control system for the Spallation Neutron Source H-source test facility Allison scanner*, Rev. Sci. Instrum. **81**, 02B722 (2010).

[12] R. D'Arcy *et al.*, *Distinct Transverse Emittance Measurements of the PXIE LEBT*, Proc. of IBIC14, Monterey, California (2014), TUPD01.

[13] J. Guyard and M. Weiss, *Use of beam emittance measurements in matching problems*, Proc. of Proton Linear Accel. Conf., Ontario, Canada (1976), AECL-5677.

[14] R. D'Arcy and A. Shemyakin, *Calculation of the effect of slit size on emittance measurements made by a two-slit scanner*, arXiv:**1503.06055** [physics.acc-ph]

[15] R. C. Connolly, *et al.*, *A correction for emittance-measurement errors caused by finite slit and collector widths*, Proc. of LINAC92, Ottawa, Canada (1992), TH4-19.